

Measurement of Differential Neutral Current Elastic ν_μ -Argon Scattering Cross Sections with MicroBooNE

MICROBOONE-NOTE-1101-PUB

The MicroBooNE Collaboration*

September 7, 2021

Abstract

The MicroBooNE experiment is an 85 ton active mass liquid-argon time projection chamber located in the Fermilab Booster Neutrino Beamline. MicroBooNE's ability to detect low-energy protons allows us to study single proton events with momenta as low as 300 MeV/c. We present a measurement of the flux-averaged neutral-current elastic differential cross section for neutrinos scattering on argon as functions of four-momentum transfer squared, Q^2 , proton kinetic energy, momentum and angle with respect to the beam direction. Our measured cross section as a function of Q^2 goes as low $Q^2 = 0.10 \text{ GeV}^2$. This is our first step towards extracting the strange quark contribution to the axial form factor, which is not only the least-constrained contribution to the neutral-current elastic scattering cross section but is also crucial for understanding the strange quark contribution to the proton spin.

*Email: MICROBOONE_INFO@fnal.gov

1 Introduction

The neutrino-proton neutral-current elastic (NCE) scattering cross section can be expressed as [1],

$$\left(\frac{d\sigma}{dQ^2}\right)_\nu^{NC} = \frac{G_F^2}{2\pi} \left[\frac{1}{2}y^2(G_M^{NC}(Q^2))^2 + (1-y - \frac{M}{2E}y) \frac{(G_E^{NC}(Q^2))^2 + \frac{E}{2M}y(G_M^{NC}(Q^2))^2}{1 + \frac{E}{2M}y} + \left(\frac{1}{2}y^2 + 1 - y + \frac{M}{2E}y\right)(G_A^{NC}(Q^2))^2 \pm 2y(1 - \frac{1}{2}y)G_M^{NC}(Q^2)G_A^{NC}(Q^2) \right],$$

where G_F is the Fermi constant, M is the mass of the nucleon, E is the neutrino energy, and Q^2 is the four-momentum transfer squared. $G_E^{NC}(Q^2)$, $G_M^{NC}(Q^2)$ and $G_A^{NC}(Q^2)$ are the neutral-current (NC) electric, magnetic, and axial form factors of the proton, respectively. The electric and magnetic form factors have been determined from the electron-nucleon elastic scattering data [2]. The axial form factor is the least known component of the cross section, especially the contribution from the strange quark.

$G_A^{NC}(Q^2)$ can be written as

$$G_A^{NC}(Q^2) = \frac{1}{2}G_A^{CC}(Q^2) + \frac{1}{2}G_A^s(Q^2), \quad (1)$$

where $G_A^{CC}(Q^2)$ is the contribution from the up and down quarks to the spin structure of the nucleon, and $G_A^s(Q^2)$ is the contribution from the strange quark. At $Q^2 = 0$, we have

$$G_A^{NC}(Q^2 = 0) = \frac{1}{2}(\Delta u - \Delta d) - \frac{1}{2}\Delta s. \quad (2)$$

$\Delta u - \Delta d = g_A$ is the weak coupling constant that has been measured in neutron decay [3]. Therefore, the neutrino-proton elastic cross section is sensitive to the value of Δs at low values of Q^2 . Past measurements have included those by E734 at BNL [4] and MiniBooNE experiment [5], however, neither was done below $Q^2 = 0.45 \text{ GeV}^2$.

In this note, we present a measurement of the flux-averaged neutral-current elastic differential cross section for neutrinos scattering on argon as a function of Q^2 from 0.1 to 1 GeV^2 .

2 MicroBooNE Experiment

The MicroBooNE [6] experiment is an 85 ton active mass liquid-argon time projection chamber (LArTPC) located at the Fermilab Booster Neutrino Beamline (BNB). The BNB is a predominantly ν_μ beam with peak energy around 600 MeV. MicroBooNE's active region is $2.3 \times 2.5 \times 10.4 \text{ m}^3$. Figure 1 shows a schematic of the MicroBooNE TPC [7]. Charged particles produced from neutrino interactions ionize the argon along their path. The ionization electrons drift in a 273 V/cm electric field along the x axis, towards the vertical (y, z) anode plane for readout.

In addition to the wire chamber, the experiment employs a set of 32 8-inch cryogenic photomultiplier tubes (PMTs) located directly behind the anode plane, in order to take advantage of the excellent scintillation properties of argon that it produces a large amount of light per unit energy deposited (about 24,000 photons per MeV at 500 V/cm drift field) and is transparent to its own scintillation. Light detected by the PMTs is used as a trigger for the presence of neutrino interactions, as well as for rejecting cosmic-ray events. This trigger looks at light activity on the PMTs in time-coincidence with the 1.6 μs beam-spill reaching the detector, which may be caused by a neutrino interaction or coincident cosmic activity.

MicroBooNE has been taking neutrino-beam data since October 2015, and has collected a total of 1.56×10^{21} protons on target (POT). In this note, we present a result using a subset (6.87×10^{20} POT) of data. Two different data streams are used in this analysis. The on-beam data stream ("BNB") is triggered by BNB neutrino spills that last for 1.6 μs . The off-beam data stream ("EXT") is taken during periods when no beam was received. The off-beam data sample is used to measure the cosmic-ray backgrounds, which are appreciable due to the location of MicroBooNE near the surface and without substantial overhead shielding.

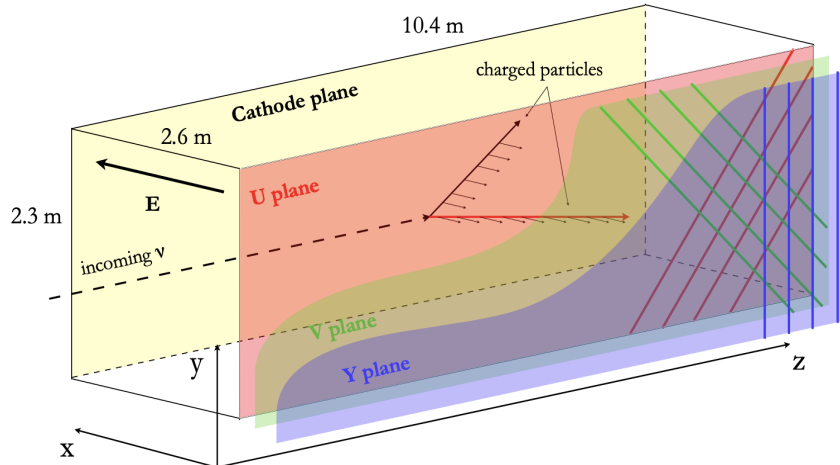


Figure 1: A schematic of the MicroBooNE TPC system from [7].

3 Neutrino Interaction Simulation

In MicroBooNE, we use a cosmic-data-overlaid Monte Carlo (MC) sample to develop the analysis. The neutrino interactions are generated using the GENIE neutrino event generator version 3.0.6 [8, 9]. We apply extra corrections to obtain a “MicroBooNE tune” [10] as our central value cross section model.

The NC models being used in the generator are summarized in Table 1. Details on all models used in GENIE and their associated uncertainties can be found in Ref. [10].

Model	Parameter	Description
Nuclear model	-	Local Fermi Gas (LFG) model
Final State Interaction Model	-	Hadron-nucleus interaction model (hA2018)
NC Elastic model	$M_A = 0.96$ GeV $\eta = 0.12$	Axial mass in Ahrens model Strange quark contribution in Ahrens model
NC Resonance model	$M_A = 1.120$ GeV $M_V = 0.840$ GeV	Axial mass of Berger-Sehgal model Vector mass of Berger-Sehgal model
NC Meson Exchange Current model	-	Empirical Dytman model

Table 1: List of models that are being used in GENIE 3.0.6 for generating neutral-current events.

4 Event Reconstruction and Selection

MicroBooNE employs signal processing [11, 12] to convert 2D raw-data into Gaussian-shaped signals (known as “hits”). We then employ the Pandora multi-algorithm pattern recognition framework [13] to convert these 2D hits into 3D objects and create a set of “Particle Flow Particles” (“PFParticles”) hierarchies, each of which corresponds to a track or shower, and their parent-daughter relationships between tracks and showers.

4.1 Proton Energy Reconstruction

The kinetic energy T (in MeV) of a candidate proton track is calculated from its track length L (in cm), using

$$T = a \cdot L^b, \quad (3)$$

in which $a = 31.3$, $b = 0.578$ are determined by fitting to the PSTAR [14] data. For protons that have kinetic energy $50 < T < 500$ MeV, their length is $2.3 < L < 115.7$ cm, according to this parameterization.

The reconstructed four-momentum transfer is determined entirely from the proton kinetic energy using

$$\begin{aligned}
 Q^2 &= -q^2 = -(p' - p)^2 \\
 &= -(E' - E)^2 + (\mathbf{p}' - \mathbf{p})^2 \\
 &= 2TM,
 \end{aligned}$$

which is valid for pure elastic scattering off a free proton, where p is four-momentum, E is energy, \mathbf{p} is three-momentum, M is proton mass, T is kinetic energy determined by the length L of the track, primed quantities refer to the final state. In a nucleus, this becomes an approximation that holds as long as the initial proton momentum is small relative to the final momentum and binding energy is small relative to the energy transfer.

4.2 Signal and Background Definitions

Our signal is defined as neutral current elastic events that produce a single proton above threshold and no other particles above threshold. We first define the category “NCE-like”. An event has to satisfy the following conditions to be considered a NCE-like event:

1. It is a muon neutrino interaction.
2. There is a proton in the final state with a momentum greater than 300 MeV/c.
3. There are no other protons in the final state with momentum greater than 300 MeV/c.
4. There are no muons or pions in the final state above their momentum thresholds of 100 MeV/c and 65 MeV/c, respectively. There can be any number of neutrons in the final state.
5. The vertex of the neutrino interaction is within the fiducial volume (FV). The FV is defined as the region 10 cm from the edges of the TPC in x and z directions and, 20 cm from the edge in y direction, excluding all the dead regions of the detector. The dead regions are defined in Appendix A .

Additionally, for this measurement we require that the event is also classed as NCE:

1. It is a true neutral current elastic interaction according to truth information
2. The struck nucleon was a proton according to truth information

The main sources of our background are

1. NCE-like background events (that are not also NCE). These events are labeled as “ ν_μ Irreducible NC1p” in the plots of this note, and are primarily due to the following categories:
 - (a) Neutral-current elastic scattering off a neutron that re-interacts in the nucleus and knocks out a proton.
 - (b) Neutral-current meson exchange current (MEC) events with one proton in the final state.
 - (c) Neutral-current resonance (RES) or deep inelastic interactions (DIS) with one proton and no other particles above threshold in the final state.
2. Protons from CC events, where the muon was not detected. These events are labeled as “CC Proton” in the plots of this note.
3. Reconstructed events coming from a cosmic-induced interaction that triggered the readout of the detector. These are modeled using random triggers with coincident cosmic activity during a false beam-window. These events are labeled as “data EXT” in the plots of this note.
4. NC proton events that have more than 1 proton in the final state, or have both proton(s) and pion(s) in the final state. These events are labeled as “NC Proton ” in the plots of this note.

5. Events in which the selected track is a cosmic track from a readout triggered by a neutrino interaction. These events are labeled as “Overlaid Cosmics” in the plots of this note.
6. Events in which the selected track is not a proton. These events are labeled as “Non-Proton” in the plots of this note.
7. Single-proton events that satisfy the signal definition, but are outside of the fiducial volume. These events are labeled as “OutFV” in the plots of this note.
8. Single-proton events that satisfy the signal definition, but are generated from $\bar{\nu}_\mu$ or ν_e events. These events are labeled as “ $\bar{\nu}_\mu$ or ν_e 0 μ 0 π 1 p Proton” in the plots of this note.

In Section 5 the second class of backgrounds “data EXT” is referred to as B_i^{EXT} , and all other backgrounds are summed together and referred to as B_i^{MC} . B_i^{EXT} is measured from data, while B_i^{MC} is estimated using the simulated samples.

4.3 Single Proton Event Selection

We require tracks to be contained in the FV, as described in Sec. 4.2. Any candidate tracks that are in or across any dead region of the detector are removed. The actual FV cuts applied could be found in Appendix A. We remove events that have more than one object in the particle-flow hierarchy, as reconstructed by Pandora, and obvious cosmic backgrounds based on the light information [15]. We only keep track candidates that are going forward along the beam direction ($\cos \theta > 0$), since the low-energy protons we are interested in tend to be forward-going. To enrich our sample in protons we only select tracks that have a deposited energy profile consistent with a proton [16].

To further reduce the cosmic background, we created a multi-class gradient-boosted decision tree (BDT) classifier using the TMVA [17] package in ROOT. The variables used for the training include the total and track-end dE/dx on the collection plane, track start and end positions in cartesian coordinates, Particle Identification (PID) variables on all planes [18], track angles, and track length. Detailed descriptions of those variables are listed in Table 2. The importance of each variable in the BDT is shown in Figure 2, it is derived by counting how often the variables are used to split decision tree nodes.

Name in Figure 2	Description
EnddEdx	Sum of dE/dx for up to the last 6 hits of a candidate track
Phi	The angle in the X-Y plane between the candidate track direction and a horizontal line pointing away from the anode
TrkDist	The ratio of distance to the closest neighboring track/length
chi2-p-2	Proton PID variable on Plane Y
chi2-p-1	Proton PID variable on Plane V
Theta	The angle between the neutrino beam and the candidate track
EndY	The end position of the candidate track in Y
chi2-p-0	Proton PID variable on Plane U
Length	Length of the candidate track
StartY	The start position of the candidate track in Y
StartZ	The start position of the candidate track in Z
TotaldEdx	Sum of dE/dx of all hits of a candidate track
EndZ	The end position of the candidate track in Z

Table 2: Description of variables in the BDT training.

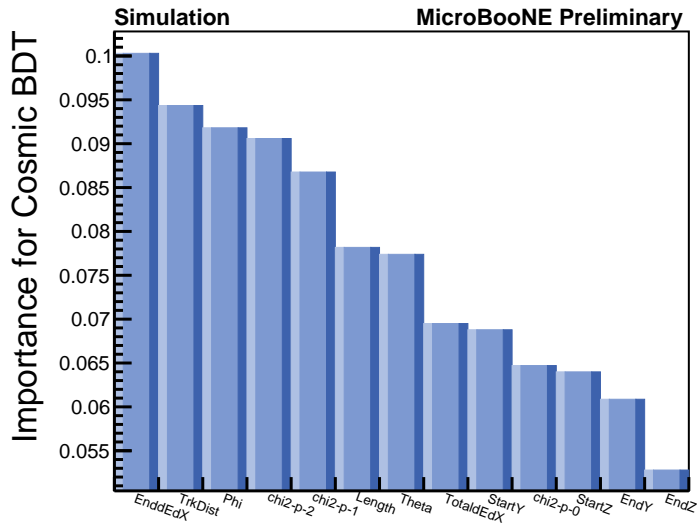


Figure 2: Importance of variables for cosmic BDT. Detailed descriptions are in Table 2.

Figure 3 shows the data-to-MC comparison of the BDT response for the candidate NCE events. We select events with BDT response above 0.2, which removes about 65% cosmic background and 10% signal events. The overall purity is 22.7% and efficiency is 37.7% in the reconstructed momentum region from 0.3 GeV/c to 1.2 GeV/c after applying the BDT cut.

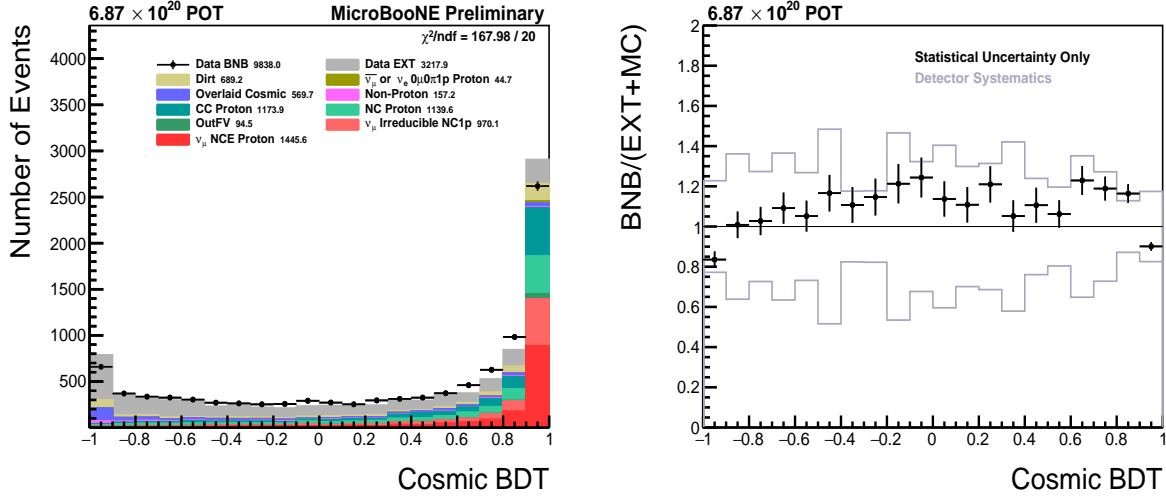


Figure 3: BDT response for Cosmic BDT (left) of the selected NCE events from Run 1-3 data and MC samples. The right plot shows the ratio of beam-on data to the prediction of the BDT response.

Figure 4 shows the reconstructed kinetic energy, T , of candidate NCE events, after the application of the BDT cut. The left plot shows the data-to-MC comparison. Figure 5, Figure 6, and Figure 7 show the reconstructed Q^2 , momentum and $\cos\theta$ of candidate NCE events, respectively.

Figure 8 shows the track start positions of the selected events.

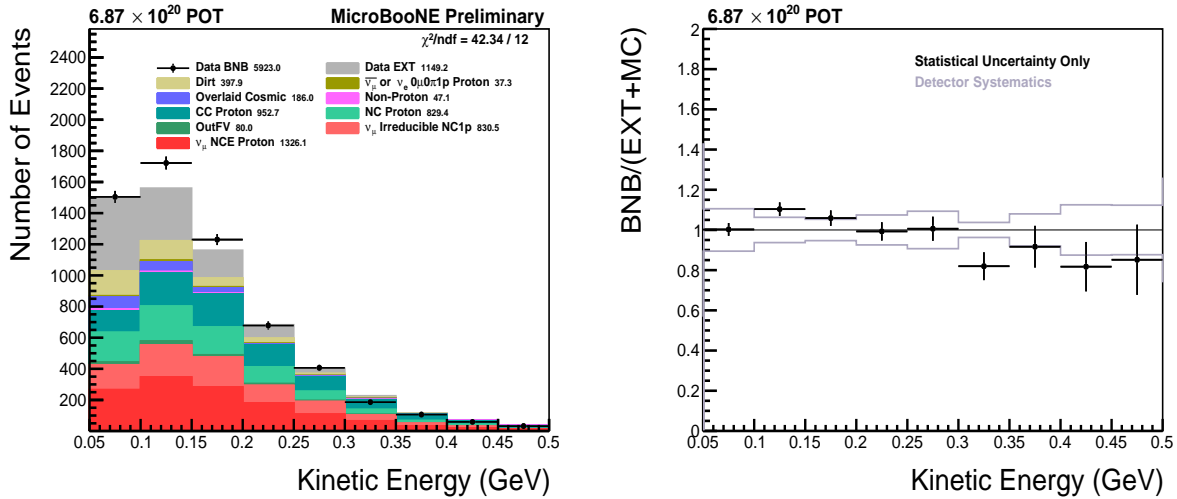


Figure 4: Reconstructed T after applying the BDT cut, from Run 1-3 data and MC samples. The stacked histograms in the left plot is broken down to highlight the NCE signals. The right plot shows the ratio of BNB/(EXT+MC).

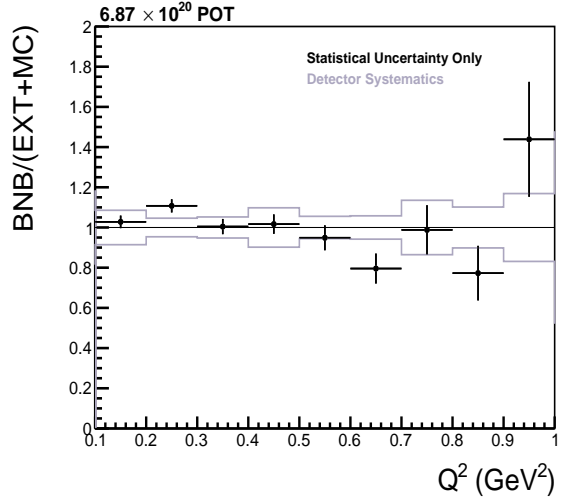
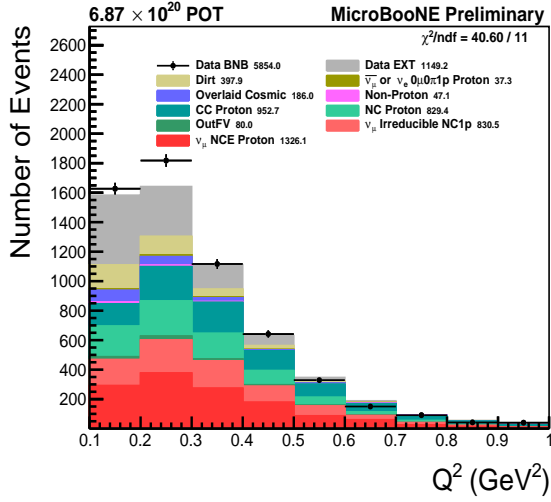


Figure 5: Reconstructed Q^2 after applying the BDT cut, from Run 1-3 data and MC samples. The stacked histograms in the left plot is broken down to highlight the NCE signals. The right plot shows the ratio of $\text{BNB}/(\text{EXT}+\text{MC})$.

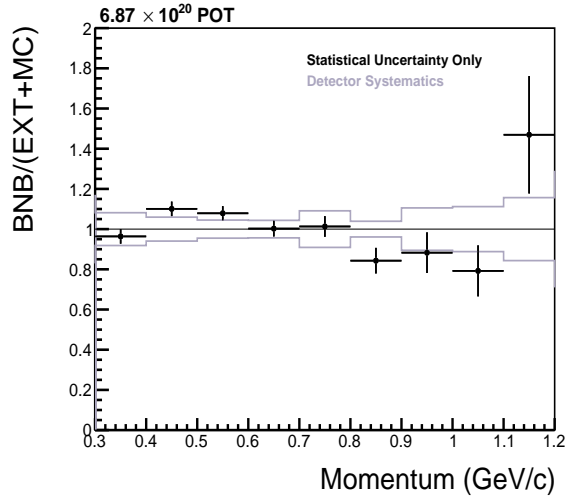
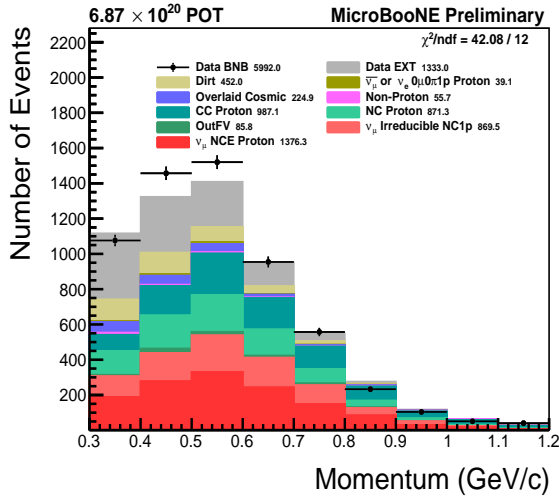


Figure 6: Reconstructed momentum after applying the BDT cut, from Run 1-3 data and MC samples. The stacked histograms in the left plot is broken down to highlight the NCE signals. The right plot shows the ratio of $\text{BNB}/(\text{EXT}+\text{MC})$.

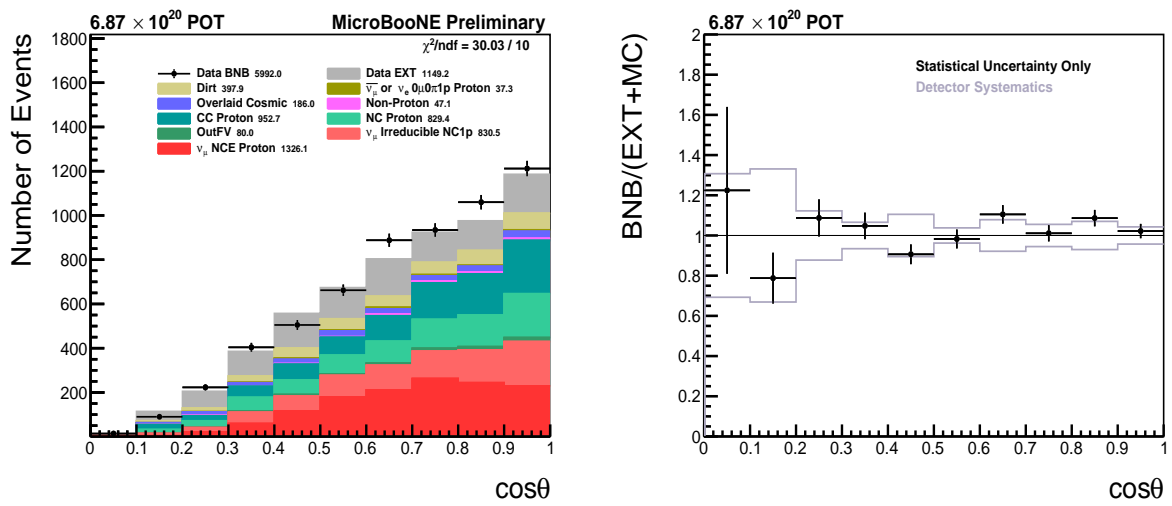


Figure 7: $\cos\theta$ distributions of the selected events after applying the BDT cut, from Run 1-3 data and MC samples.

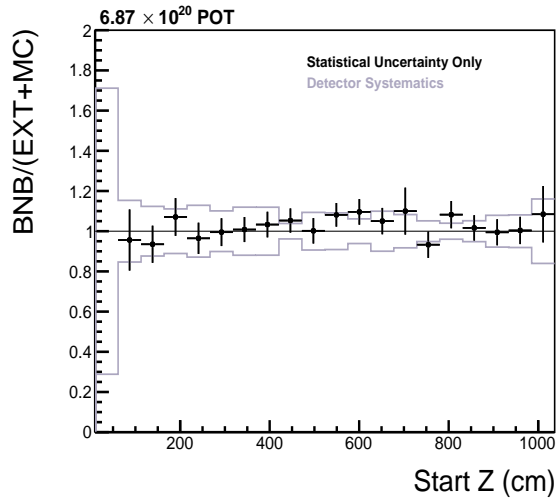
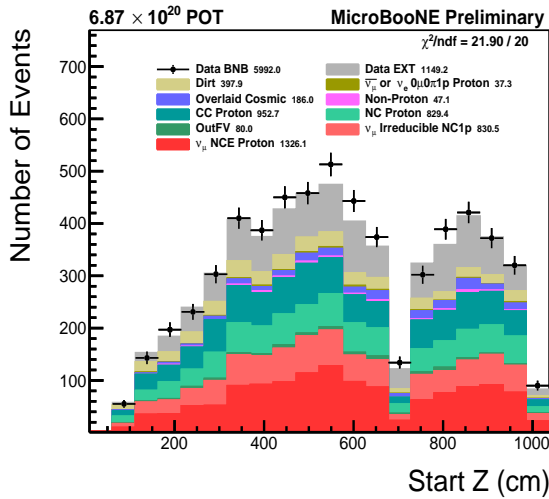
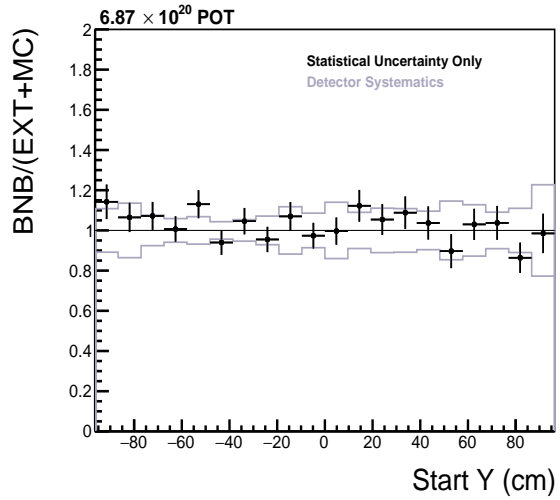
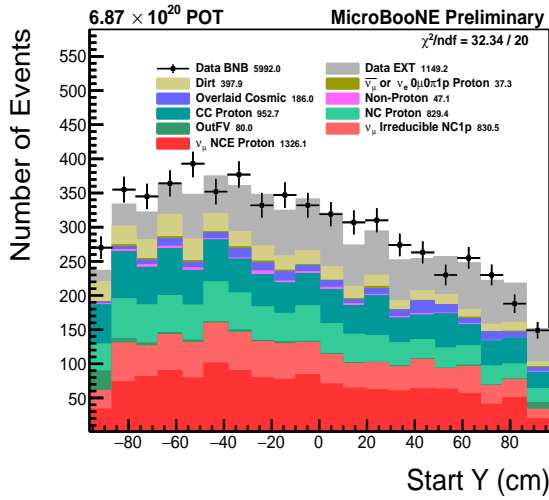
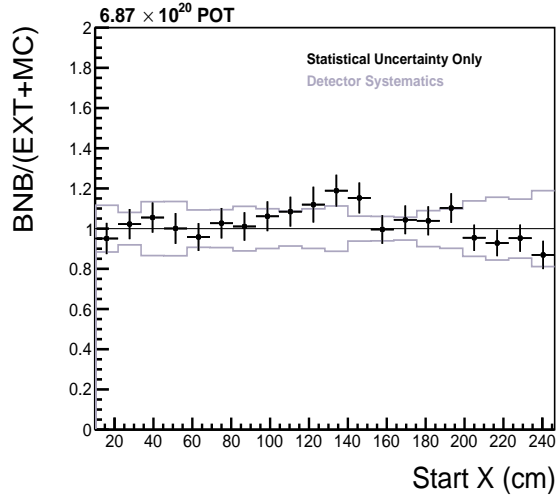
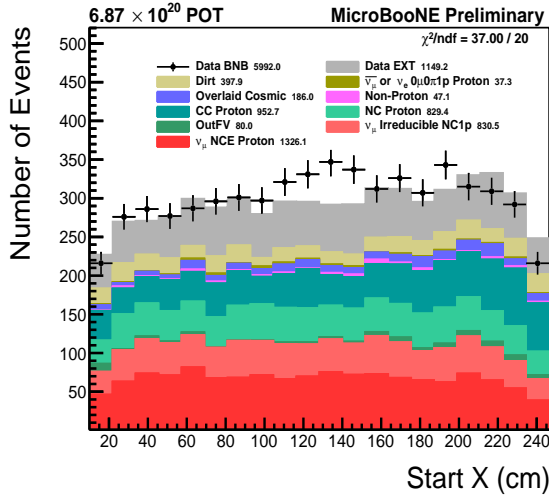


Figure 8: Track start x , y , and z distributions of the selected events.

5 Differential Cross Section Extraction

We extract differential cross section $d\sigma/dx$ in true x (with x stands for kinetic energy T , Q^2 , momentum p or $\cos\theta$) using unfolding method. We unfold using the D'Agostini iterative unfolding algorithm as found in the RooUnfold [19] package. We find that one iteration is sufficient to produce a stable result so a single iteration is used for all differential cross sections.

The differential cross section can be written as

$$\left(\frac{d\sigma}{dx}\right)_i = \frac{S_i^{\text{unfolded}}}{\epsilon_i \cdot N_{\text{target}} \cdot \Phi_{\nu_\mu} \cdot (\Delta x)_i} \quad (4)$$

in which i is the i -th true x bin, S_i^{unfolded} is the unfolded background-subtracted event rate that is produced from $N_j - B_j$ in the reconstructed space. N_j is the event rate in the j -th reconstructed bin, $B_j = B_j^{\text{EXT}} + B_j^{\text{MC}}$ is the background in bin j , where B_j^{MC} and B_j^{EXT} are the backgrounds that have been defined in Section 4.2. ϵ_i is the efficiency correction in bin i , as defined in Eq. 5.

$$\epsilon_i = \frac{N_i^{\text{selected}}}{N_i^{\text{generated}}} \quad (5)$$

where N_i^{selected} is the number of selected true signal events and $N_i^{\text{generated}}$ is the generated signal events in the same bin.

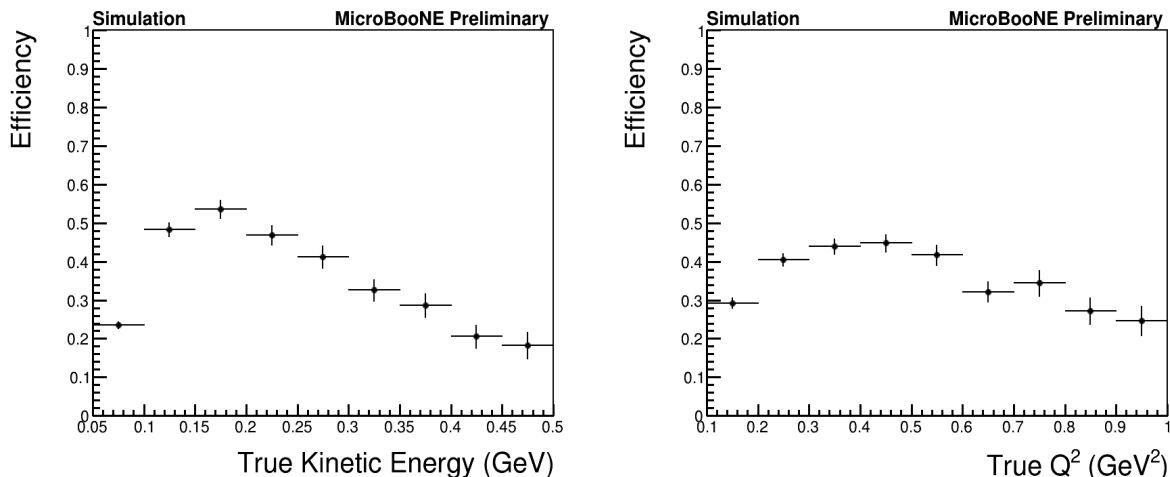


Figure 9: Left: efficiency correction in true kinetic energy T . Right: efficiency correction in true Q^2 .

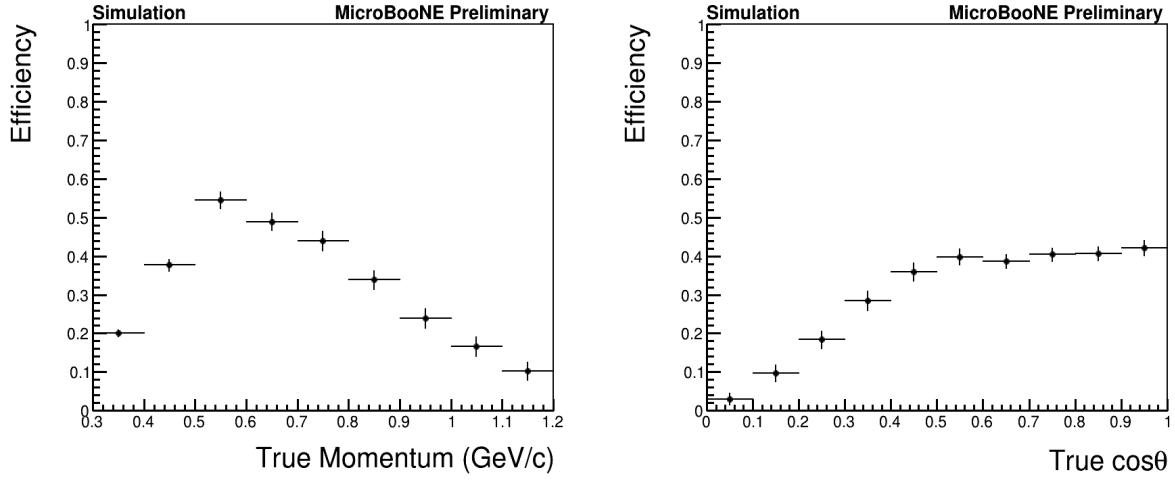


Figure 10: Left: efficiency correction in true momentum. Right: efficiency correction in true $\cos\theta$.

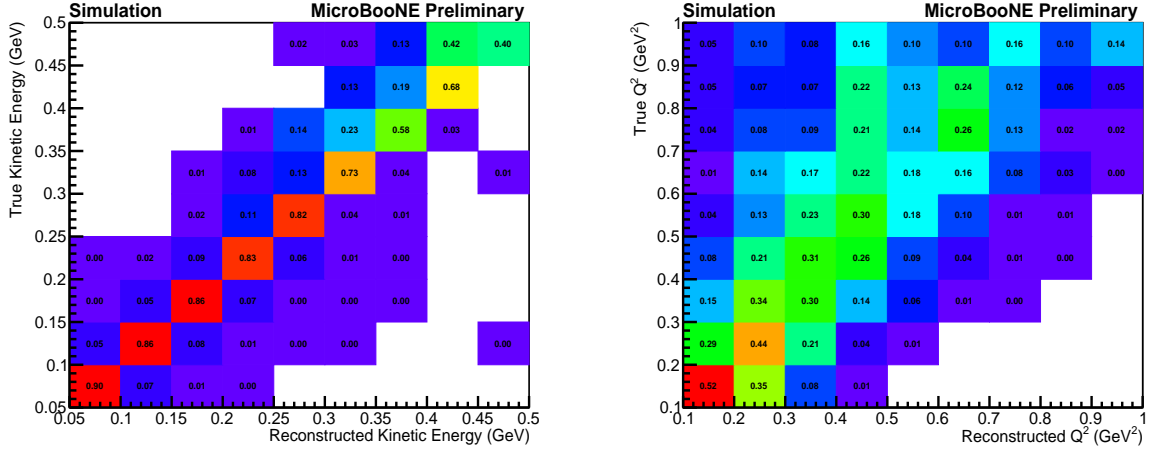


Figure 11: Smearing matrices used in the unfolding procedure for $d\sigma/dT$ (left) and $d\sigma/dQ^2$ (right). Both matrices are normalized by row.

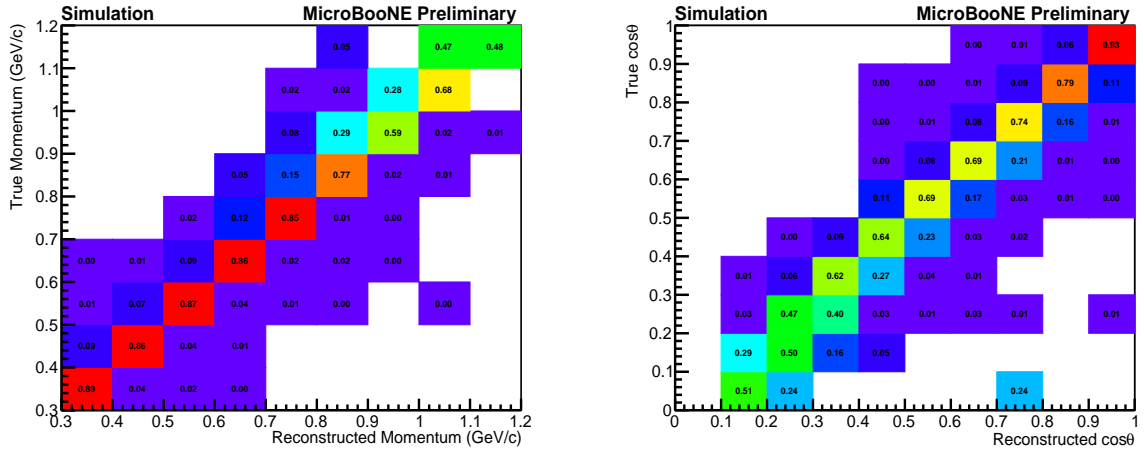


Figure 12: Smearing matrices used in the unfolding procedure for $d\sigma/dp$ (left) and $d\sigma/d\cos\theta$ (right). Both matrices are normalized by row.

The number of target protons N_{target} is defined as

$$N_{\text{target}} = \rho_{\text{Ar}} \cdot V_{\text{Ar}} \cdot N_A \cdot N_{\text{protons}}/m_{\text{mol}} \quad (6)$$

In which $\rho_{\text{Ar}} = 1.3836 \text{ g/cm}^3$, V_{Ar} is the fiducial volume, $m_{\text{mol}} = 39.95 \text{ g/mol}$, $N_A = 6.022140857(74) \cdot 10^{23} \text{ molecules/mol}$, $N_{\text{protons}} = Z = 18$, the number of protons in the ^{40}Ar nucleus.

The integrated flux is calculated to be $\Phi_{\nu\mu} = 3.87 \times 10^{11} \text{ cm}^{-2}$. The bin width $(\Delta x)_i$ is $(\Delta T)_i = 0.05 \text{ GeV}$, $(\Delta p)_i = 0.1 \text{ GeV}$ or $(\Delta \cos\theta)_i = 0.1$ for all the bins.

6 Systematic Uncertainties

Four main sources of systematic uncertainties are considered in this measurement: neutrino beam flux predictions, neutrino interaction modeling, detector modeling and modeling of secondary hadronic interaction that happens after the primary neutrino interaction.

The neutrino beam flux uncertainty comes from the uncertainties in the production of secondary particles when the BNB protons from the primary beam collide with the beam-target, as well as the uncertainties from the magnetic horn current, the depth by which the current penetrates the conductor, and the interactions of secondary particles with the target and surrounding material [20, 21].

The neutrino interaction modeling uncertainties are evaluated using the GENIE [8] reweighting framework. The sources of uncertainty are summarized in Ref. [10], which include variations of the NC and CC interaction models and the Final State Interaction (FSI) model. This type of uncertainty is still preliminary, as currently, we do not have any uncertainty on the shape of the NCMEC background, which is an important component of the irreducible background and therefore would affect the shape of the measured cross section.

The secondary hadronic interaction uncertainties come from the uncertainties of the cross section of a hadron’s interaction with argon nuclei as the particles traverse the detector’s medium, which could change the type and kinematics of the detected final-state particles. The uncertainties being considered include π^+ , π^- , proton and neutron re-interactions, where we assume a 20% normalization uncertainty on the elastic and inelastic scattering cross sections used for secondary interactions in the GEANT4 [22] detector simulation software. These uncertainties are also preliminary and work is underway to understand neutron re-interaction uncertainties in more detail [23].

Most of the detector modeling uncertainties are evaluated using a data-driven approach that directly modifies the simulation of the signal response as a function of the particles true kinematics [24]. It is based on a data-driven data-MC comparison, which then is propagated to the reconstructed events by modifying the deconvolved wire waveforms. Light yield (LY) variations are another type of detector-related uncertainties which take into account the overall LY drop, the variation of Rayleigh scattering length, and light attenuation length to account for drift-distance-dependent mismodeling. We also consider the variation of the values of the input parameters α and β used in the Modified Box model [25]. In addition, uncertainty on our characterization of the electric-field non-uniformity - known as space-charge effect (SCE) [26], the modification of the electric field due to accumulated charge from slow moving ions - is evaluated by using an alternative E -field map.

The systematic uncertainties on the differential cross section are evaluated by re-extracting the differential cross section with varied background, efficiency correction, and integrated flux terms.

For the neutrino interaction modeling, secondary re-interaction modeling and beam flux uncertainties, we use the “multisim” technique, which consists of generating several MC samples, each one called a “universe” with parameters in the models varied within their uncertainties, also taking into account correlations [10]. We re-extract the cross section σ^s from each universe s . The mean of the cross sections from the N_s universes is defined as

$$m_i = \frac{1}{N_s} \sum_s \sigma_i^s. \quad (7)$$

Where i stands for the i -th bin. The uncertainty E_i in the i -th bin is defined as

$$E_i = \sqrt{V_i + B_i}, \quad (8)$$

where

$$V_i = \frac{1}{N_s} \sum_s (\sigma_i^s - m_i)^2, \quad (9)$$

and

$$B_i = (\sigma_i^{cv} - m_i)^2. \quad (10)$$

V_i represents the spread in bin contents around the mean of the universes and B_i represents the overall bias of the mean of the universes with respect to σ^{cv} , which is the cross-section extracted in a given bin using the nominal simulation.

For detector-related uncertainties, the fractional difference from the central value cross section is assigned as the systematic uncertainty.

Figure 13 and Figure 14 show the summary of the systematic uncertainties of the differential cross sections $d\sigma/dT$, $d\sigma/dQ^2$, $d\sigma/dp$, and $d\sigma/d\cos\theta$. The neutrino interaction model uncertainty dominates in almost all bins, which is mostly propagated from the MC background component. The low statistics at the high-energy and $\cos\theta < 0.3$ bins cause the overestimation of the uncertainty.

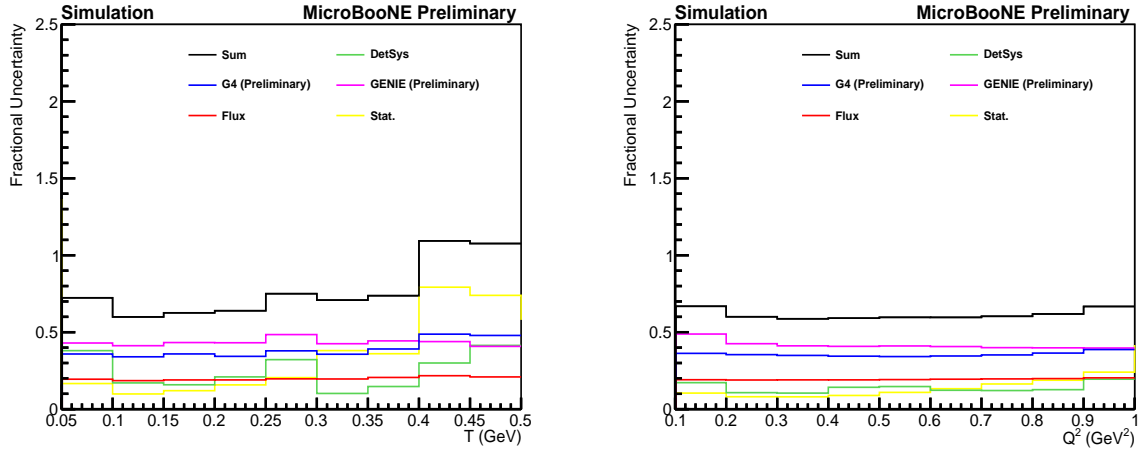


Figure 13: Summary of systematic uncertainties on the measured differential cross sections $d\sigma/dT$ and $d\sigma/dQ^2$. The asymmetry of the total systematic uncertainty comes from the detector-simulation component.

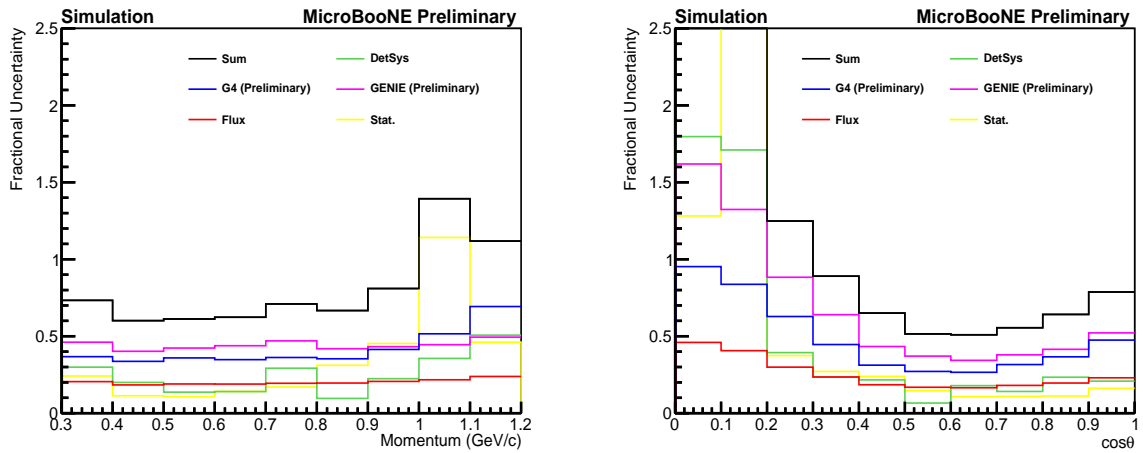


Figure 14: Summary of systematic uncertainties on the measured differential cross sections $d\sigma/dp$ and $d\sigma/d\cos\theta$. The asymmetry of the total systematic uncertainty comes from the detector-simulation component.

7 Results and Outlook

Figure 15 and Figure 16 show the final differential cross sections with all uncertainties added in quadrature, with the total uncertainty ranging from 50% to 100% at high energies. The cross sections extracted from data and MC agree within 1σ in all bins.

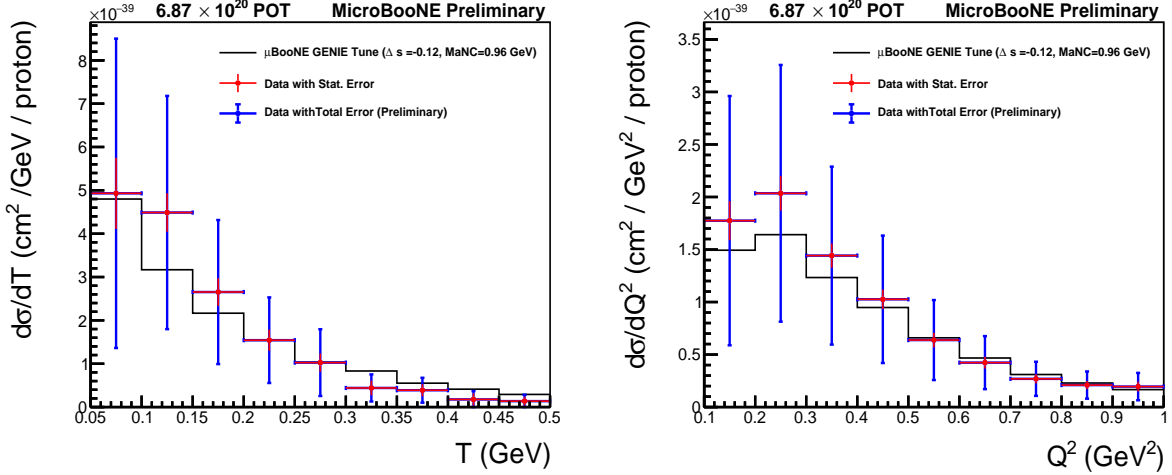


Figure 15: Final differential cross sections $d\sigma/dT$ and $d\sigma/dQ^2$ with both statistical and systematic uncertainties.

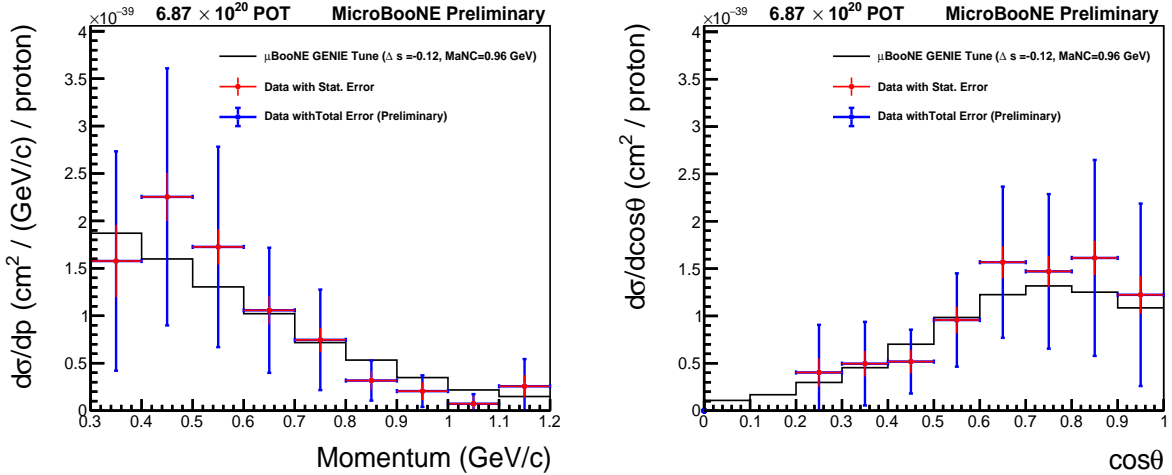


Figure 16: Final differential cross sections $d\sigma/dp$ and $d\sigma/d\cos\theta$ with both statistical and systematic uncertainties.

Several improvements will be carried out to improve this analysis in the near future:

1. We will update the binning of the cross sections to improve the stability of unfolding in regions with limited statistics. Number of iterations used in the unfolding procedure will also be re-evaluated once the new binning is chosen.
2. We will work to better evaluate uncertainties on irreducible backgrounds, such as NC MEC, as well as improving the treatment of neutron re-interaction uncertainties. Additionally, we will update the

axial form factor in GENIE from the dipole shape to “ z -expansion” in NC Elastic cross section, which is a model-independent, and systematically improvable, representation of axial form factor [27].

3. We will try to improve the selection purity. Currently, we apply a conservative BDT cut to obtain a relatively high efficiency at low Q^2 region, since the low- Q^2 events are precious to us. By tightening the BDT cut, we could further increasing the purity, therefore reduce the systematic uncertainty that comes from the predicted background events.

We present the first measured NCE differential cross sections on argon using 6.87×10^{20} POT beam-on data. The differential cross section $d\sigma/dQ^2$ goes as low as $Q^2 = 0.1 \text{ GeV}^2$, which is significantly lower than previous measurements [4, 28] in neutrino experiments. With the above improvements, we hope to extract the strange axial form factor with a greater precision than previous measurements in neutrino experiments.

A Containment Cuts

The containment cuts are shown in Figure 17. The whole Y-Z grey region stands for the whole TPC. The five purple regions are the fiducial regions used in this measurement where all three wire planes are active.

In the signal definition, we require the vertex of a signal event to be within one of the five purple regions.

During event selection, a reconstructed track is required to be contained in one of the five purple regions. Any candidate tracks that are in or across any gray region of the detector will be removed. The area of the five purple regions makes up 57.7% of the whole TPC in the Y-Z view.

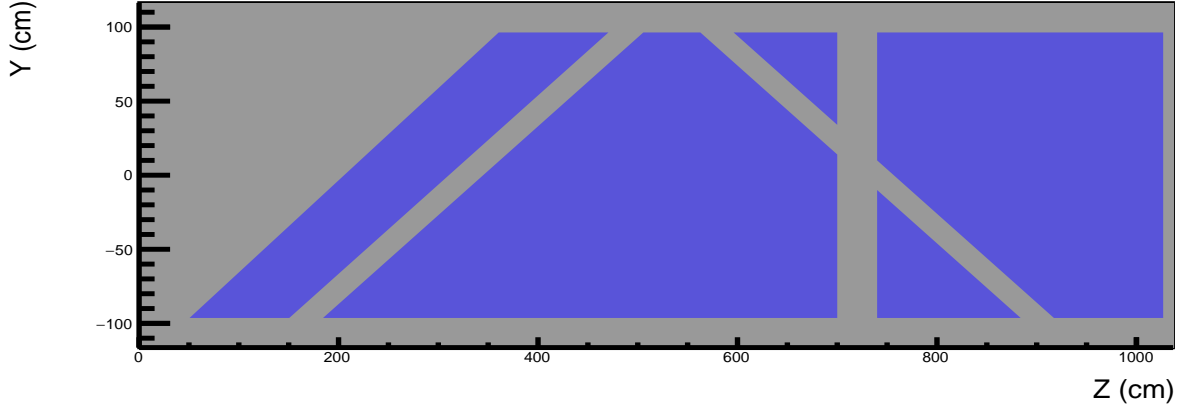


Figure 17: Fiducial cuts applied on the single proton candidates. The grey region stands for the whole TPC. A track is required to be contained in one of the five purple regions, where all three wire plane are active. Any tracks that are in or across any of the regions of the detector colored grey will be removed.

To select a coordinate (st_x, st_y, st_z) that is within the FV as shown in Figure 17, we require

“VertexIsInFV(st_x , st_y , st_z) > 0”.

This C++ function is defined as below.

```

Int_t VertexIsInFV(float st_x, float st_y, float st_z)
{
    int passFV=0;
    const float xmin=0;
    const float xmax=256.35;
    const float ymin=-116.35;
    const float ymax=116.35;
    const float zmin=0;
    const float zmax=1036.8;
    const float border_xorz=10;
    const float border_y=20;
    if(st_x < xmin+ border_xorz) passFV=-1;
    if(st_y< ymin + border_y) passFV=-1;
    if(st_z< zmin + border_xorz) passFV=-1;
    if(st_x > xmax - border_xorz) passFV=-1;
    if(st_y > ymax - border_y) passFV=-1;
    if(st_z > zmax - border_xorz) passFV=-1;
    if(st_y -0.6*st_z>-186&&st_y -0.6*st_z<-120) passFV=1;
    if(st_y -0.6*st_z<-207&&st_y +0.6*st_z<434&&st_z <700) passFV=2;
    if(st_z >740&&st_y +0.6*st_z >454) passFV=3;
    if(st_y +0.6*st_z >454&&st_z <700) passFV=4;
    if(st_y +0.6*st_z <434&&st_z >740) passFV=5;
}

```

```
    return passFV;
}
```

References

- [1] W. M. Alberico, Samoil M. Bilenky, and C. Maieron. Strangeness in the nucleon: Neutrino - nucleon and polarized electron - nucleon scattering. *Phys. Rept.*, 358:227–308, 2002.
- [2] J. Arrington, W. Melnitchouk, and J. A. Tjon. Global analysis of proton elastic form factor data with two-photon exchange corrections. *Phys. Rev. C*, 76:035205, 2007.
- [3] Nicola Cabibbo, Earl C. Swallow, and Roland Winston. Semileptonic hyperon decays. *Ann. Rev. Nucl. Part. Sci.*, 53:39–75, 2003.
- [4] L.A. Ahrens et al. Measurement of Neutrino - Proton and anti-neutrino - Proton Elastic Scattering. *Phys. Rev. D*, 35:785, 1987.
- [5] A. A. Aguilar-Arevalo et al. Measurement of the Neutrino Neutral-Current Elastic Differential Cross Section on Mineral Oil at $E_\nu \sim 1$ GeV. *Phys. Rev. D*, 82:092005, 2010.
- [6] R. Acciarri et al. Design and Construction of the MicroBooNE Detector. *JINST*, 12(02):P02017, 2017.
- [7] P. Abratenko et al. Vertex-Finding and Reconstruction of Contained Two-track Neutrino Events in the MicroBooNE Detector. 2 2020.
- [8] C. Andreopoulos et al. The GENIE Neutrino Monte Carlo Generator. *Nucl. Instrum. Meth. A*, 614:87–104, 2010.
- [9] Costas Andreopoulos, Christopher Barry, Steve Dytman, Hugh Gallagher, Tomasz Golan, Robert Hatcher, Gabriel Perdue, and Julia Yarba. The GENIE Neutrino Monte Carlo Generator: Physics and User Manual. 10 2015.
- [10] The MicroBooNE collaboration. Neutrino Interaction Model and Uncertainties for MicroBooNE Analyses. <https://microboone.fnal.gov/public-notes>, MICROBOONE-NOTE-1074-PUB.
- [11] C. Adams et al. Ionization electron signal processing in single phase LArTPCs. Part I. Algorithm Description and quantitative evaluation with MicroBooNE simulation. *JINST*, 13(07):P07006, 2018.
- [12] C. Adams et al. Ionization electron signal processing in single phase LArTPCs. Part II. Data/simulation comparison and performance in MicroBooNE. *JINST*, 13(07):P07007, 2018.
- [13] R. Acciarri et al. The Pandora multi-algorithm approach to automated pattern recognition of cosmic-ray muon and neutrino events in the MicroBooNE detector. *J. Phys. Conf. Ser.*, 888(1):012142, 2017.
- [14] <https://physics.nist.gov/PhysRefData/Star/Text/PSTAR.html>.
- [15] The MicroBooNE collaboration. Measurement of ν_e Interactions at Low Energy with the MicroBooNE Experiment. <https://microboone.fnal.gov/public-notes>, MICROBOONE-NOTE-1085-PUB.
- [16] The MicroBooNE collaboration. Selection of numu charged-current induced interactions with $N > 0$ protons and performance of events with $N = 2$ protons in the final state in the MicroBooNE detector from the BNB. <https://microboone.fnal.gov/public-notes>, MICROBOONE-NOTE-1056-PUB.
- [17] A. Hoecker, P. Speckmayer, J. Stelzer, J. Therhaag, E. von Toerne, H. Voss, M. Backes, T. Carli, O. Cohen, A. Christov, D. Dannheim, K. Danielowski, S. Henrot-Versille, M. Jachowski, K. Kraszewski, A. Krasznahorkay Jr., M. Kruk, Y. Mahalalel, R. Ospanov, X. Prudent, A. Robert, D. Schouten, F. Tegenfeldt, A. Voigt, K. Voss, M. Wolter, and A. Zemla. Tmva - toolkit for multivariate data analysis, 2007.

- [18] P. Abratenko et al. Measurement of differential cross sections for ν_μ -Ar charged-current interactions with protons and no pions in the final state with the MicroBooNE detector. *Phys. Rev. D*, 102(11):112013, 2020.
- [19] <https://gitlab.cern.ch/RooUnfold/RooUnfold>.
- [20] A. A. Aguilar-Arevalo et al. The Neutrino Flux prediction at MiniBooNE. *Phys. Rev.*, D79:072002, 2009.
- [21] The MicroBooNE collaboration. Booster Neutrino Flux Prediction at MicroBooNE. <https://microboone.fnal.gov/public-notes>, MICROBOONE-NOTE-1031-PUB.
- [22] S. Agostinelli et al. GEANT4: A Simulation toolkit. *Nucl. Instrum. Meth. A*, 506:250–303, 2003.
- [23] J. Calcutt, C. Thorpe, K. Mahn, and L. Fields. Geant4reweight: a framework for evaluating and propagating hadronic interaction uncertainties in geant4. *Journal of Instrumentation*, 16(08):P08042, aug 2021.
- [24] The MicroBooNE collaboration. Novel Approach for Evaluating Detector Systematics in the MicroBooNE LArTPC. <https://microboone.fnal.gov/public-notes>, MICROBOONE-NOTE-1075-PUB.
- [25] R. Acciarri et al. A Study of Electron Recombination Using Highly Ionizing Particles in the ArgoNeuT Liquid Argon TPC. *JINST*, 8:P08005, 2013.
- [26] The MicroBooNE Collaboration. Measurement of space charge effects in the MicroBooNE LArTPC using cosmic muons. *Journal of Instrumentation*, 15(12):P12037–P12037, dec 2020.
- [27] Aaron S. Meyer, Minerba Betancourt, Richard Gran, and Richard J. Hill. Deuterium target data for precision neutrino-nucleus cross sections. *Phys. Rev. D*, 93(11):113015, 2016.
- [28] A.A. Aguilar-Arevalo et al. Measurement of the Neutrino Neutral-Current Elastic Differential Cross Section on Mineral Oil at $E_\nu \sim 1$ GeV. *Phys. Rev. D*, 82:092005, 2010.